

Retraction

Retracted: The Clinical Value of CT Scans for the Early Diagnosis and Treatment of Spinal Fractures and Paraplegia

Journal of Healthcare Engineering

Received 23 May 2023; Accepted 23 May 2023; Published 24 May 2023

Copyright © 2023 Journal of Healthcare Engineering. This is an open access article distributed under the Creative Commons Attribution License, which permits unrestricted use, distribution, and reproduction in any medium, provided the original work is properly cited.

This article has been retracted by Hindawi following an investigation undertaken by the publisher [1]. This investigation has uncovered evidence of one or more of the following indicators of systematic manipulation of the publication process:

- (1) Discrepancies in scope
- (2) Discrepancies in the description of the research reported
- (3) Discrepancies between the availability of data and the research described
- (4) Inappropriate citations
- (5) Incoherent, meaningless and/or irrelevant content included in the article
- (6) Peer-review manipulation

The presence of these indicators undermines our confidence in the integrity of the article's content and we cannot, therefore, vouch for its reliability. Please note that this notice is intended solely to alert readers that the content of this article is unreliable. We have not investigated whether authors were aware of or involved in the systematic manipulation of the publication process. Wiley and Hindawi regrets that the usual quality checks did not identify these issues before publication and have since put additional measures in place to safeguard research integrity.

We wish to credit our own Research Integrity and Research Publishing teams and anonymous and named external researchers and research integrity experts for contributing to this investigation.

The corresponding author, as the representative of all authors, has been given the opportunity to register their agreement or disagreement to this retraction. We have kept a record of any response received.

References

- [1] P. Jia, S. Zhu, and L. Guo, "The Clinical Value of CT Scans for the Early Diagnosis and Treatment of Spinal Fractures and Paraplegia," *Journal of Healthcare Engineering*, vol. 2021, Article ID 6672091, 11 pages, 2021.

Research Article

The Clinical Value of CT Scans for the Early Diagnosis and Treatment of Spinal Fractures and Paraplegia

Peng Jia,¹ Shan Zhu,² and Lin Guo ²

¹Orthopaedic Trauma, Tianjin Hospital, Tianjin 300350, China

²Radiology Department, Tianjin Hospital, Tianjin 300350, China

Correspondence should be addressed to Lin Guo; anna@tjfsu.edu.cn

Received 16 December 2020; Revised 27 January 2021; Accepted 4 February 2021; Published 13 February 2021

Academic Editor: Zhihan Lv

Copyright © 2021 Peng Jia et al. This is an open access article distributed under the Creative Commons Attribution License, which permits unrestricted use, distribution, and reproduction in any medium, provided the original work is properly cited.

The early diagnosis and treatment of spinal fractures and paraplegia by CT scan is investigated in depth and its clinical value is discussed in this paper. In this paper, a novel circulatory generation adversarial network, Spine-GAN, is proposed for the diagnosis of various spinal diseases. The algorithmic model can fully automate the segmentation and classification of multiple spinal structures, such as intervertebral discs, vertebrae, and neuroforamina, simultaneously to intelligently generate a complete clinical diagnosis. The innovation of this method is that Spine-GAN not only overcomes the high variability and complexity of spinal structures in MRI images but also preserves the subtle differences between normal and abnormal spinal structures and dynamically learns obscure but important spatial pathological relationships between adjacent structures of the spine, thus overcoming the limitations of small datasets. Spine-GAN enables accurate segmentation, radiological classification, and pathological correlation representation of the three spinal diseases. Specifically, Spine-GAN achieves a pixel accuracy of 96.2% with a specificity and sensitivity distribution of 89.1% and 86%, respectively. The DMML-Net and Spine-GAN algorithm models have important applications and research values in the clinical diagnosis of spinal diseases and MRI image processing, as well as in the intelligent generation of medical image diagnostic reports, which are of great importance for the study of fine-grained image classification of pathological images. It also has a positive impact on the development of the software.

1. Introduction

The spine is the central axis of the trunk and is composed of many vertebrae that are not rigidly joined. It contains four physiological curves: cervical, thoracic, lumbar, and caudal [1]. The canine spine is divided into five vertebral regions: seven cervical (C7), thirteen thoracic (T13), seven lumbar (L7), three sacral (sacrum) (S3), and caudal (Cd variables). The vertebrae are complex structures consisting of vertebral bodies, vertebral roots, and various load-bearing structures such as transverse processes, spinous processes, articular processes, collaterals, and papillae [2]. The vertebral body is broadly cylindrical with a slightly flattened dorsal surface, a convex head, and a concave tail. The vertebral arch consists of two upright vertebral roots on the left and right and the vertebral plates connecting them, forming a spinal canal surrounding the spinal cord. The spinal cord, which is part of

the central nervous system, is cylindrical, connected to the medulla oblongata, and extends continuously within the spinal canal, terminating at approximately the level of the fifth lumbar vertebra and containing both cervical and lumbar expansion [3]. There are incisions in the vertebral roots and in the continuous bony joints these combine to form the intervertebral foramen, which is the opening through which the spinal nerves and the blood vessels that provide structure to the spinal canal pass [4].

The vertebral body-bearing areas are specific structures such as spines, articulations, and transverse processes. Each part of the vertebrae is composed of cortical and cancellous bones, which vary in density and structure. The cortical bone is cortical, which provides cortical bone strength but limited flexibility, and the cancellous bone is composed of trabeculae, which are avascular bone structures. The trabeculae are surrounded by fatty tissue and hematopoietic space, which

includes the bone marrow [5]. Although AS with spinal fracture is not a complication, the trauma that causes the fracture is often mild, even without obvious trauma, so it is easily missed or misdiagnosed clinically, and when missed or misdiagnosed, it can often lead to serious consequences such as nerve damage [6]. Routine x-ray, CT, and MRI have their advantages and disadvantages for the diagnosis of AS with spinal fracture. X-rays are inexpensive and have less radiation and can be used as a basic screening test; CT can clarify the type of fracture and spinal stability, whereas MRI has the highest sensitivity and can show minor bone contusion and enema changes [7]. It prevents serious adverse consequences and has a tremendous diagnostic value that is irreplaceable by other screening methods [8].

Kurkure and Thakare categorized tibial plateau fractures as collapsed, non-displaced, split fracture, and split collapse, which Howl expanded into non-displaced, partially compressed, split collapsed, total condylar fracture, split, and comminuted [9]. Schatzki classifies tibial plateau fractures into the following six types: Type I: simple split fracture of the lateral condyle; Type II: split with compression fracture; Type III: simple central compression fracture; Type IV: medial condyle fracture; Type V: bicondylar fracture; Type VI: complete fracture of the tibia with metaphysis [10]. As each type of Schatzki's classification has similar injury mechanism and imaging manifestations, the increase in classification grade often implies an increase in injury energy, difficulty in management, and the possibility of poor prognosis, which is of great significance for clinical diagnosis and treatment [11]. Based on CT, Patil et al. divided the tibial plateau into three sectors and classified tibial plateau fractures into zero-column fractures (simple compression fractures), single-column fractures, double-column fractures, and triple-column fractures. Their study showed a significant correlation between this classification and treatment decisions, which is becoming widely accepted [12]. The Schatzki classification was refined into 6 types and 18 subtypes by combining CT scan; Krause divided the tibial plateau into 10 parts based on the AO/OTA classification and 3D-CT results and proposed the ten-segment classification. The fracture was divided into the medial column, intermediate column, lateral column, and fibular column, and then each column was subdivided, and the "four columns and nine zones" classification was proposed [13]. By adding the number of columns and zones [14] involved in the fracture, the authors obtained the "tibial plateau injury index" to assess the degree of injury of the patient, which has some clinical significance [15]. These three types of staging avoid the disadvantage of missed diagnosis of posterior condylar fractures, but their staging is too complex and their relevance to treatment and prognosis needs further study. Imaging is the most important method for the evaluation of tibial plateau fractures; plain x-rays are convenient and easy to perform, but are easily missed; CT and 3D reconstruction can reveal microfractures and non-displaced fractures of the tibial plateau, which has become indispensable in the diagnosis of tibial plateau fractures; CT is of great significance in the evaluation of soft tissue injuries such as ligaments and menisci, plays an important role in guiding treatment and

postoperative rehabilitation, and is recommended for all patients. MRI should be performed in patients with tibial plateau fractures to assess soft tissue injury [16].

In summary, there has been extensive research on the evaluation of AS mobility, and both clinical evaluation parameters and imaging parameters have their advantages and disadvantages. The most common are fractures caused by spine involvement and joint deformities caused by peripheral joint involvement. CSD-CNN is a nonlinear representation learning model that turns the feature extraction step into a feature learning step and bypasses the need for manual feature engineering methods, using an end-to-end training approach that automatically learns semantic and discriminative hierarchical features from low to high levels. To overcome the obstacles in histological images of pathology, CSD-CNN is designed with intra- and inter-class feature space relationships in mind. In particular, the feature space distance is a measure of image similarity, but the feature space distance of the same class of samples may be larger than that of different classes of samples. Therefore, in this paper, some feature space distance constraints are integrated into CSD-CNN to control the feature similarity of different types of histopathological images.

2. Study of CT Scans for Spinal Fractures with Paraplegia

2.1. CT Scan Technical Description. X-ray utilization was extremely low, scanning time was long, and motion artifacts were severe. It was limited to cranial examinations [17]. The second generation of CT machines uses the same translational/rotational scanning method for scanning and information acquisition as the first generation, except that the pencil x-ray beam of the first generation has been replaced with a small-angle fan x-ray beam, the scanning range has been increased, and the number of detectors has been increased to improve image quality and shorten scanning time. The third generation of CT machines uses monitoring detectors, a rotating/rotating scanning method, and an increased angle of the fan x-ray beam, and a significantly higher number of detectors than the second-generation machines [18]. This dramatically shortens the scan cycle time to 50 milliseconds per scan and reduces artifacts during cardiac scans, improving image quality, as shown in Figure 1.

CTV is a new type of three-dimensional reconstruction technique in which the images obtained from a multi-layer spiral CT scan are transferred to a workstation and post-processed by a computer system to reconstruct a stereoscopic image of a cavity organ. It is a new three-dimensional reconstruction technique. CTV can simulate the morphology of the inner wall of the duct and visually reflect the internal lesions, especially for some occupying lesions [19]. At present, CTVE is more commonly used in the clinical examination of the intestine and trachea. X-rays are converted into images based on their attenuation coefficient in the material. In addition to the morphological display, specific tissue identification can be performed. High- and low-energy data acquisition can be performed instantaneously, and a single-energy reconstruction of the two

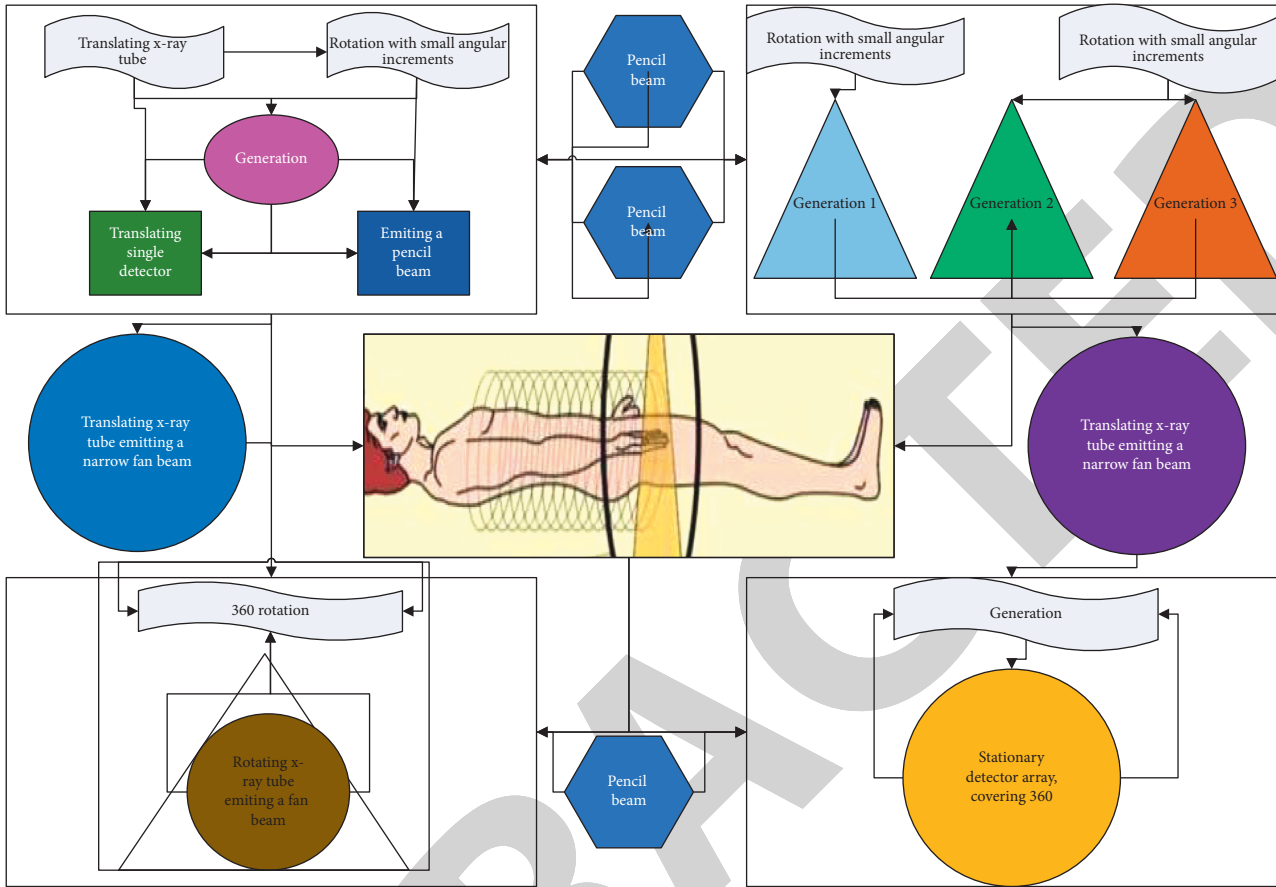


FIGURE 1: Q-WSEM model in IoT environment CT scanning technology schematic structure.

acquired datasets can be performed using the original data projection. By acquiring dual-energy data and performing spectroscopic analysis of the results, not only can morphologically changes in tissues and organs be obtained, but also material separation, extraction of proton density maps, anhydrous iodine maps, etc. can be achieved, and optimal energy imaging can be obtained. This is an important step in the development of CT. The clinical application of spectral CT is based on techniques that optimize image quality and contrast-to-noise ratio.

The staging of tibial plateau fractures plays a critical role in both clinical practice and academic communication. An ideal fracture typing should not only reflect the mechanism and degree of injury, and can guide treatment and determine prognosis, but also be simple to use and easy to communicate and have a high degree of consistency. Over the past few decades, multiple staging systems have been proposed for tibial plateau fractures, such as the Howl, Moore, Schatzki, and AO/OTA staging systems based on fracture morphology, the Khan staging system based on fracture line location, the CT-based three-column, four-column, ten-column, four-nine-column, and the injury-based three-column, four- and nine-column staging systems, and the CT-based three-column, four-column, ten-column, four-nine-column, and four-nine-column staging systems. The Schatzki classification has been used to determine the mechanism of injury and the type of injury. The Schatzki

classification of each type has similar injury mechanism and imaging manifestations, and with the increase of classification grade, the injury energy increases, the handling difficulty increases, and the possibility of poor prognosis increases, which is important for clinical diagnosis and treatment. With the widespread application of CT technology in fracture diagnosis, CT-based three-column typing has been increasingly used in clinical practice.

2.2. Analytical Methods for Design Analysis. In this study, three staging methods were used. (1) Schatzki staging: proposed by Schatzki in 1979, the tibial plateau was divided into the following six types based on plain x-rays: Type I: splitting fracture of the lateral condyle alone; Type II: splitting with compression fracture. (2) Type III: compression fracture of the central condyle alone; Type IV: medial condyle fracture; Type V: bicondylar fracture; Type VI: tibial plateau fracture with complete fracture of the diaphysis (Figure 1). (3) CT-based three-column classification: proposed by Config Luo in 2010, the tibial plateau is divided into three sectors based on CT, and the tibial plateau is classified based on the fracture line involving the cortex of the corresponding region. Fractures were divided into zero-column fractures (simple compression fractures), single-column fractures, double-column fractures, and three-column fractures as shown in Figure 2.

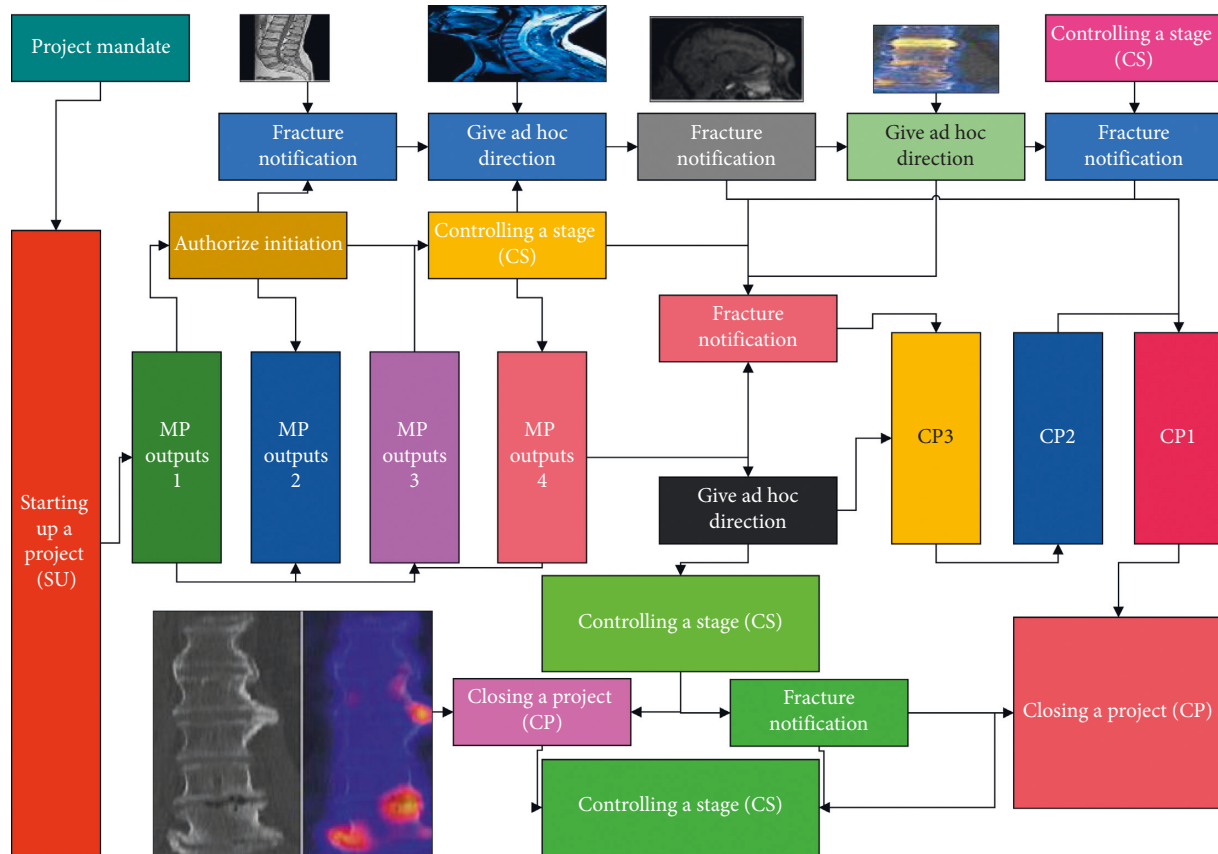


FIGURE 2: Schematic diagram of the initial map of ROI and reconstruction of a pseudo-color map for CT placement.

The study was conducted by two physicians (Observer A and Observer B) who were trained in tibial plateau fracture typing and began the study after passing the examination. Both physicians independently performed all case typing, withholding medical history, and providing only imaging data [20]. Two months later, the cases were randomly sequenced by IBM SPSS Statistics 23 software, and both again independently typed all the cases. This study used Microsoft Excel software to record the raw data for all typing and IBM SPSS Statistics 23 software to statistically analyse the data.

The validity of the three types of typing was evaluated by their agreement rates. The Kappa values were calculated using cross-tabulations and graded using the Landis and Koch criterion, and their reliability was evaluated by analysing the reliability and repeatability of the three types. The agreement rate and Kappa values were tested using the independent samples *t*-test, and the binary variables were tested using the karate-squared test, and $p < 0.05$ was considered statistically significant.

All cases underwent routine laboratory tests, mainly including CRP, ESR, and HLA-B27, and MRI was performed within one week after the laboratory tests [21]. BASDAI score was performed according to the clinical symptoms of the patients. All clinical data were recorded in Excel 2016. All cases were divided into active and resting groups according to the clinical data (CRP, ESR, BASDAI score). Active group: CRP >10 mg/L, ESR >15 mm/h in men, >20 mm/h in women or BASDAI score >6 ; resting group: CRP <10 mg/L,

CRP <10 mg/L, ESR >15 mm/h in men, >20 mm/h in women or BASDAI score >6 . ESR <15 mm/h, females <20 mm/h or BASDAI score <4 ; BASDAI score 4–6 are the suspicious activity periods, which were grouped with the image data, as shown in Table 1.

Before DCE scan, scan a series of sequences with different inversion angles ($2^\circ, 15^\circ$; the same parameters as above, scan-only one temporal phase). The contrast was injected at the end of the second temporal phase during the DCE-CT scan using Onegin (Gd-DTPA-BMA), using a high-pressure syringe at a dose of 0.1 mmol/kg at an injection flow rate of 2.0 ml/s, and pushed with 10 ml of saline after injection. The oblique coronal plane is parallel to the long axis of the sacrum (S2-3 plane), which is the most used image plane for sacroiliitis-related studies.

Image analysis and data measurement of DCE-CT and DWI images of the sacroiliac joint were performed independently by two experienced radiologists (>5 years of experience in diagnostic imaging) each. The data were sent to GE Omni-Kinetics (V 2.06) software for postprocessing. Selection of the region of interest (ROI): the ROI was placed below the articular surface of the iliac and sacral sides of the sacroiliac joint, adjacent to the cortex or cartilage, with four regions at each level, and multiple consecutive levels of measurement averaged. During the selection of the ROI, the areas of cortical bone, blood vessels, necrosis, and capsular changes were avoided. The PKMs parameter K_{trans} (volume-transfer constant; permeability of the contrast agent

TABLE 1: Recommended scheme perfusion parameters.

256-row spiral CT	14	Netherlands Philips
Contrast agent	175	Non-ionic contrast agent iohexol, specification 370 mg/ml
3D precision surgery planning and analysis system	45	China NCOOL Medical Technology Company
Windows 8 operating system	77	American Microsoft Corporation
SPSS22.0 software	88	1
256-row single-source dual-energy CT (Revolution CT)	54	American GE
AW4.6 workstation	12	American GE
Double barrel high-pressure syringe	18	Urich, Germany

from the vessel to the extracellular vascular space) of DCE-CT was measured within the ROI. The selection of the ROI for the measurement of the ADC values of DWI was the same as described above.

2.3. Analytical Methods for Design Analysis. Record the CT dose index (CTDI) and dose length product (DLP) from the radiation dose report automatically generated by the scanner after the CTP scan of the examinee. Calculate the effective radiation dose (ED) using the formula

$$m_1 = m_1 = 2 \left[\frac{(ta + tb)^{2\delta}}{\delta} \right]^2, \quad (1)$$

$$TD = DLP \times k. \quad (2)$$

The above radiation dose parameters divided by the number of samples is the corresponding value of the radiation dose of a single sample, multiplied by the adjusted number of samples is the corresponding value of the radiation dose parameters of the four groups. The bronchial tree is observed and analysed according to the branching type, diameter, and direction of travel of each bronchial tube, and the corresponding data are evaluated comprehensively. If the number of crests at the bifurcation is one, then the corresponding bronchial tree is of the two-opening type; if the number of crests is two and both crests are at the same level, then the corresponding bronchial tree is of the three-opening type.

The perfusion parameter data obtained from four different time sampling methods were analysed by the test of normality, and none of them conformed to the normal distribution, so they were expressed as median (range). Points within a 95% CI are expressed as a percentage (total number of points/dots that fall within the 95% CI). The subjective image quality of the two radiologists was tested for consistency using the Kappa test ($k < 0.2$ for very poor consistency; $0.2 < k < 0.4$ for fair consistency; $0.4 < k < 0.6$ for moderate consistency; $0.6 < k < 0.8$ for good consistency; $0.8 < k < 1$ for very good consistency). The radiation dose parameters were analysed by the normal test for normal distribution, so they were expressed as mean \pm standard deviation and analysed by the independent samples *t*-test. The test level (α) was 0.05, as shown in Table 1, which is the recommended solution for the perfusion parameters.

As shown in Figure 3, 5 of the 60 subjects were diagnosed with haemorrhagic foci, 4 had a history of surgery, and 47 subjects were finally enrolled, including 33 males and 14

females, aged 61 ± 9 years. 19 patients (11 males) in the AIS group and 28 patients (22 males) in the group without AIS were examined, and 10 ROIs were placed in the ischemic region and the contralateral brain parenchyma at the same site in each patient in the AIS group. In the AIS group ($n = 190$), the BF, BV, and MTT were 40.68, 10.29, and 10.68, respectively. The differences between the two groups were statistically significant ($Z = -16.30, -9.90, -14.65$, p -value all < 0.01). In Figure 3, the results of the between-group analysis showed that, in patients with AIS, BF was increased in group 2 compared to group 1, MTT was shortened in group 4 compared to group 1, and MTT was shortened in group 4 compared to group 1. In Figure 3, it is shown that, for patients without AIS, the MTT in group 4 was shorter than that in group 1, with a statistically significant difference ($Z = -2.44$, p -value < 0.01), while the difference between group 2 and group 3 was not statistically significant (p -value > 0.05). The differences between BF, BV, and MTT in group 3 were not statistically significant compared with group 1 (p -value > 0.05). Combining the results of all the parameters of the enrolled subjects, there were no statistically significant differences in BF, BV, and MTT in group 3 compared with group 1 (p -value > 0.05).

3. Results Analysis

3.1. Analysis of Experimental Design Results. The proposed DMML-Net has been thoroughly evaluated on a challenging dataset of 200 clinical patients (average age 60 years). Because these patients from multiple centres are examined by medical devices from multiple vendors (GE, Siemens), the generated CTs have different repetition times, echo times, magnetic fields, planar resolution, and slice thicknesses. Thus, the dataset has 200 lumbar spine CTs from 200 patients, so no patient appears in both the training (80%) and testing (20%) sets. Because each lumbar spine scan has 6 neural foramina, 6 intervertebral discs, and 5 intervertebral discs from T12 to S1, the dataset has 1200 neural foramina (518 normal, 682 abnormal), 1200 intervertebral discs (627 normal, 573 abnormal), and 1000 lumbar vertebrae (690 normal, 310 abnormal). An experienced physician annotated these CT images. Standard fivefold cross-validation was used for performance evaluation and comparison. Also, data enhancement methods were used to generalize the model. DMML-Net was implemented in python 3.6 and TensorFlow 3.0 libraries. The learning rate was 0.01 and the optimizer was Adam. gradient attenuation was 0.9 and 0.0005, respectively. The training model was trained using Nvidia GPU Titan X and Conn V5.1 and Intel CPU Xeon (R) E5-

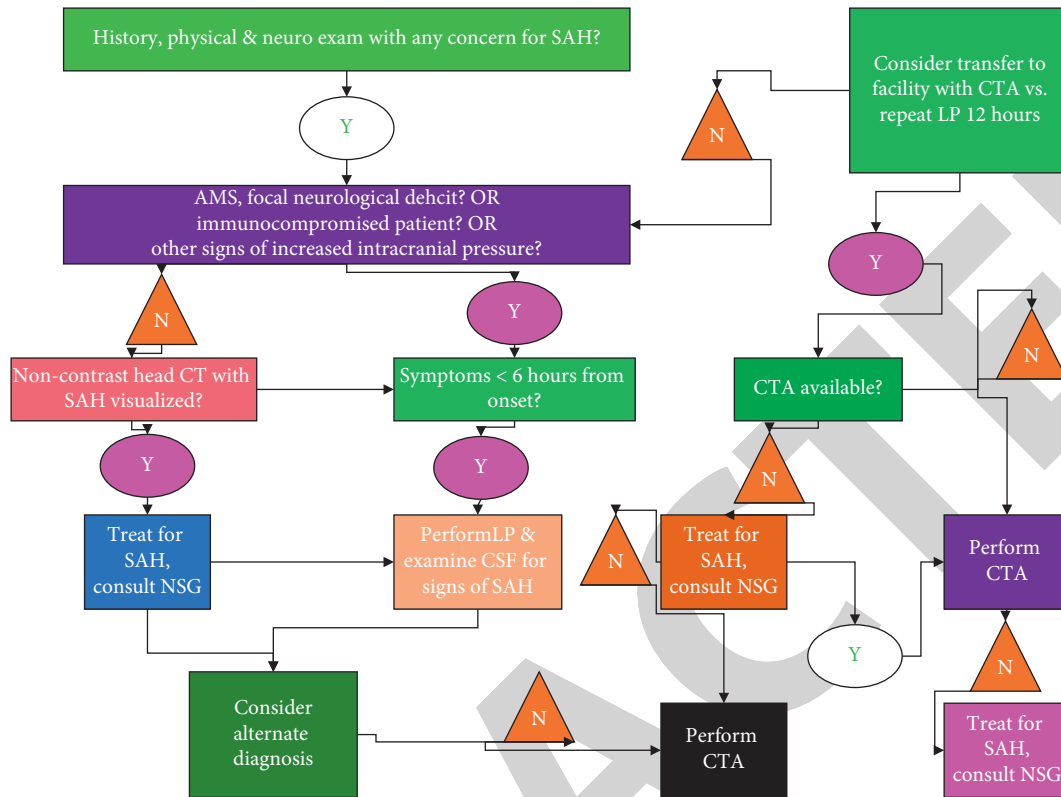


FIGURE 3: Diagnostic evaluation design.

2620@2.5 GHz with a training batch size of 8, and a gradient attenuation of 0.9 and 0.0005, respectively. The maximum number of iterations is 10k and the result is shown in Figure 4.

The input to the unsupervised labelling process is a prediction map generated by RGAN, and the output is three dictionaries containing the position and category (normal or abnormal) of three spinal structures. The key of each dictionary is the position of one type of structure, while the value of the dictionary is the normal condition for the position of one type of structure in the lumbar spine. The first step in the unsupervised labelling process is to discover the pattern of position assignment for each pixel. According to the observations in this paper, local correlation and peripheral correlation are inherent patterns within lumbar structures; i.e., in the lumbar spine, all intervertebral discs are spaced by order like a piano blank. In the case of intervertebral discs, for example, this paper first calculates the minimum height of the vertebral body and then divides the height by 4 as the boundary between the disc pixels. Thus, the marginal pixels of the intervertebral discs are placed on the list in this paper. Since the generated map has several points, the second step is to determine the true labels of the edge pixels. For example, at the L5-S1 disc, this paper compares the number of pixels between the normal and abnormal labels and then selects the one with the most pixels as the final label. The results are collected in a dictionary for use in the next report generation process. The inputs to this report generation process are three dictionaries and the output is a complete structural radiology report. Although

there are always different styles and patterns of reports written by different radiologists, the focus remains on the clinical problem. After summarizing the common patterns in radiology reports as decision problems, this article can be used to create a single template using the If-Then notation operation, as shown in Figure 5.

These three modules give Spine-GAN superior performance for dissection and radiographic classification of intervertebral discs, neuroforamina, and neuroforamina. As a baseline, Spine-GAN achieved an average of $96.02\% \pm 0.3$ -pixel accuracy, $87.01\% \pm 1.00$ Dice coefficient, $89.10\% \pm 1.70$ specificity, and $86.00\% \pm 1.70$ sensitivity. After retaining only, the ACAE module, pixel accuracy and Dice coefficient were $95.8\% \pm 0.2$ and $84.1\% \pm 1.3$, respectively, a decrease of 0.4% and 3.0%, respectively. This demonstrates not only the effectiveness of the Local-LSTM module, CNN module, but also the ability of the ACAE module to obtain deep semantic expressions and preserve the fine-grained details of the differences between normal and anomalous structures. The concept of deep learning comes from the research of artificial neural networks. The multi-layer perceptron with multiple hidden layers is a deep learning structure. Deep learning forms a more abstract high-level representation attribute category or feature by combining low-level features to discover distributed feature representations of data. Then, after removing the CNN module without generating an adversarial training, the pixel accuracy and Dice coefficients were $95.9\% \pm 0.2$ and $84.8\% \pm 0.9$, respectively, a decrease of 0.3% and 2.3%, respectively, indicating that the CNN module is effective in correcting false semantic

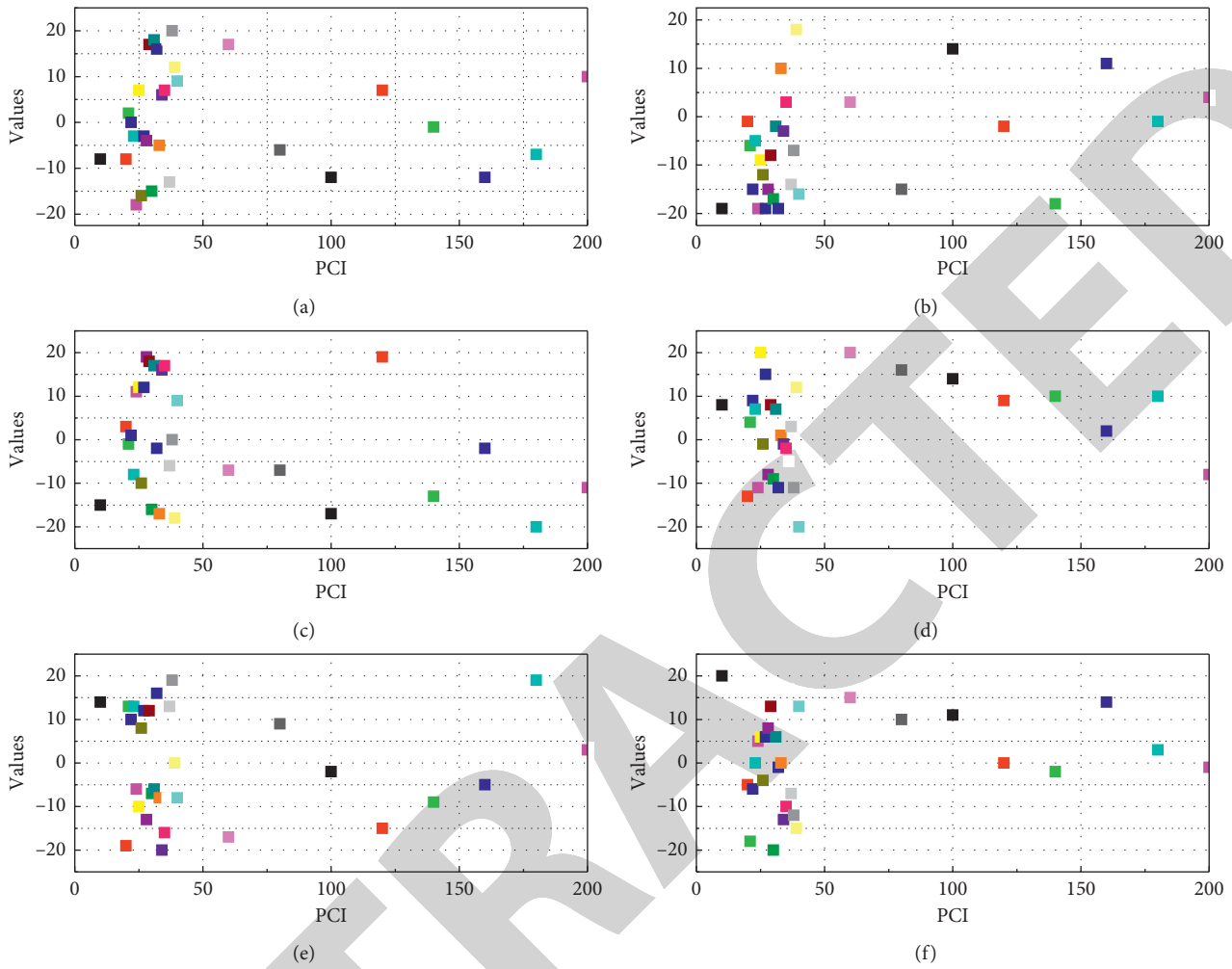


FIGURE 4: Schematic representation of recall and accuracy curves.

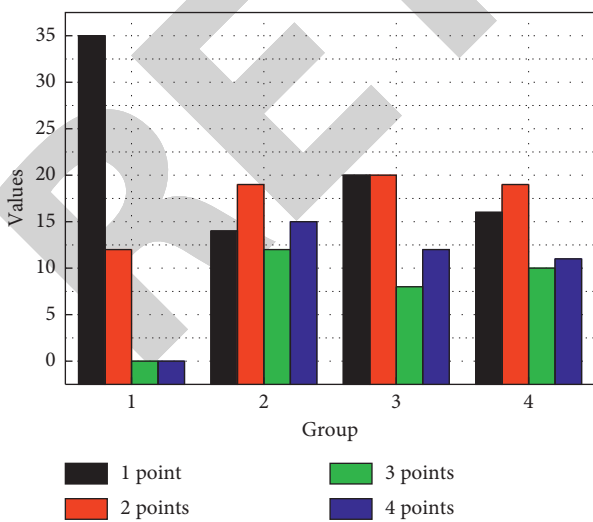


FIGURE 5: Statistical comparison chart.

segmentation. Finally, the removal of the Local-LSTM module resulted in specificity and sensitivity of $87.3\% \pm 0.02$ and $85.5\% \pm 0.03$, a decrease of 1.8% and 0.5%, respectively,

demonstrating the ability of the Local-LSTM module to simulate the spatial pathological relevance of the surrounding anomalies. The representative feature map in Figure 5 is a better visualization of the ability of the Local-LSTM module to model the spatial correlation between vertebrae, intervertebral discs, and the neuroforamina. Also, Spine-GAN has a higher specificity and sensitivity regarding radiological classification. Therefore, the combination of the ACAE module, the Local-LSTM module, and the CNN module makes Spine-GAN an effective and reliable resolution for semantic segmentation of multiple spinal structures, as shown in Figure 6.

Concerning the Local-LSTM module, since the output of the encoder network is divided into smaller parts and fed sequentially into the LSTM, the order and size of the parts will affect the performance of the semantic segmentation of multiple spine structures. Therefore, this paper conducts several comparative experiments based on different orders and sizes. First, the order of the final network parts in this paper is from top-left to bottom-right (top-down). This order is determined because the spinal structure itself has a top-down spatial correlation, which can be used in LSTM to learn a priori knowledge to improve semantic segmentation

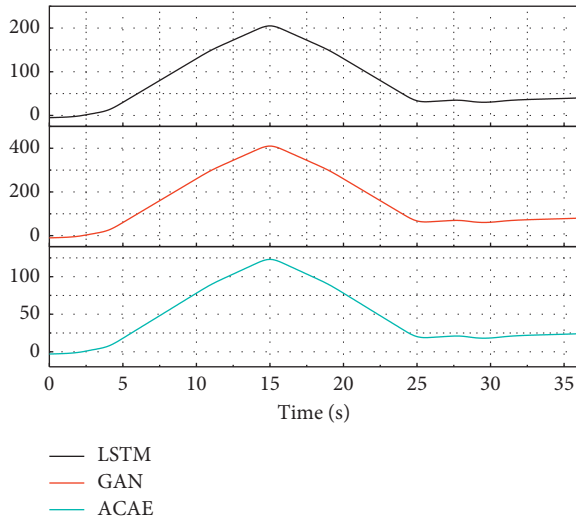


FIGURE 6: Comparison of results.

performance. In this paper, three comparative experiments were conducted on the top-down, bottom-up, and bidirectional orders. The results show that top-down achieves the best performance, as shown in Figure 7. Second, the size of each component is 4×4 . The reason for the size determination is that 4×4 was found to be the most appropriate size for the received field of each filter in the previous convolutional layer of the Local-LSTM module after the actual size statistics were calculated in this paper. The effect of the spine structure on the MR image was calculated for the receptive field of each filter of the previous convolutional layer. In this paper, three comparison experiments were performed, with sizes of 2×2 , 4×4 , and 8×8 . The results show that the 4×4 size achieves the best performance, as shown in Figure 7.

Spine-GAN combines the advantages of powerful Atreus convolution and autoencoders for semantic fine-grained representation, leverages LSTM features to model spatial pathological relationships between abnormal spinal structures, and relies on auxiliary CNN modules to correct prediction errors [22]. When validated against spine MR images from 253 patients, Spine-GAN achieves accurate segmentation, radiological classification, and pathological correlation representation of the three spinal diseases. Specifically, Spine-GAN achieved a pixel accuracy of 96.2%, demonstrating that the system in this paper provides a very intuitive representation for clinical applications. Spine-GAN has a specificity of 89.1% and sensitivity of 86% for all three types of spinal structures, indicating that the system can help clinicians improve their diagnostic efficiency.

3.2. Diagnosis and Treatment Clinical Outcome Analysis. The general information and clinical parameters of all cases are shown in Figure 8. A total of 32 cases were included in the study, and 30 cases were HLA-B27 positive, with a positive rate of 93.75%. The remaining 31 cases involved both sides, and 4 cases had osteoarthritis of the sacroiliac joint. In 18 active cases, bone marrow enema was found

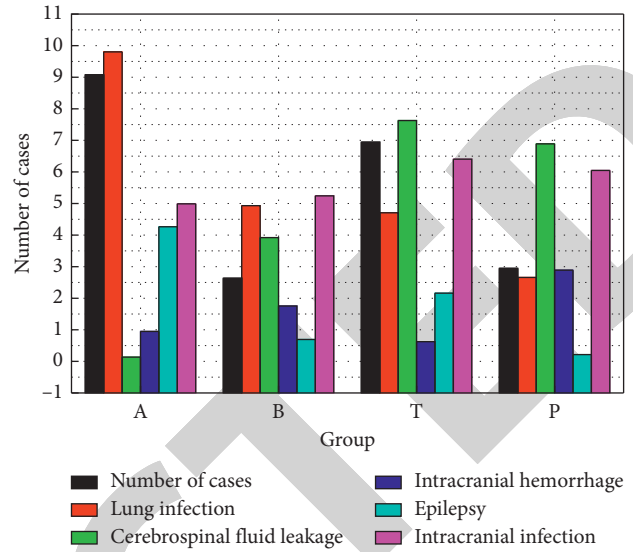


FIGURE 7: Generated feature map.

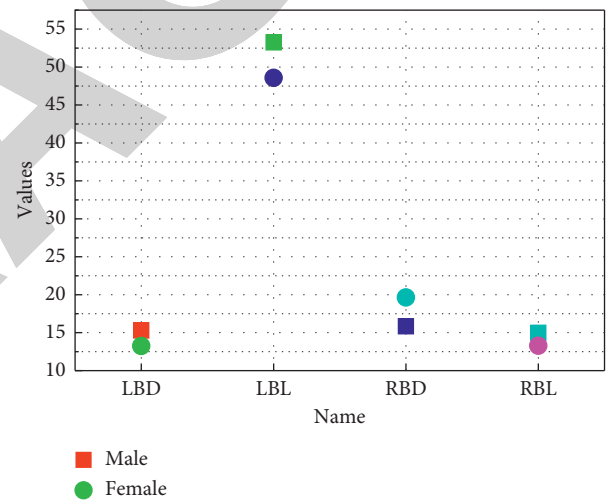


FIGURE 8: Comparison of general information and clinical parameters between the active and resting groups.

under the articular surface, and after CT enhancement, the area of subchondral bone marrow enema was found to be significantly enhanced, and DWI images could also be observed to have increased signal in the corresponding area.

After the intraoperative fluoroscopic image and preoperative CT have been successfully matched, the robot is placed in the appropriate fixed-frame rail position according to the workstation instructions. The workstation guides the robot precisely to the predetermined position according to the introduced preoperative plan and then places the corresponding robotic arm and trocar assembly, drills the holes, places the guidewire, and confirms the position of the guidewire by orthotopic fluoroscopy. After the patient is anesthetized, take a prone position and keep the abdomen suspended, sterilize the towel with the responsible segment as the center, install the robot and bedside rail, determine the responsible segment under x-ray positioning, take a picture

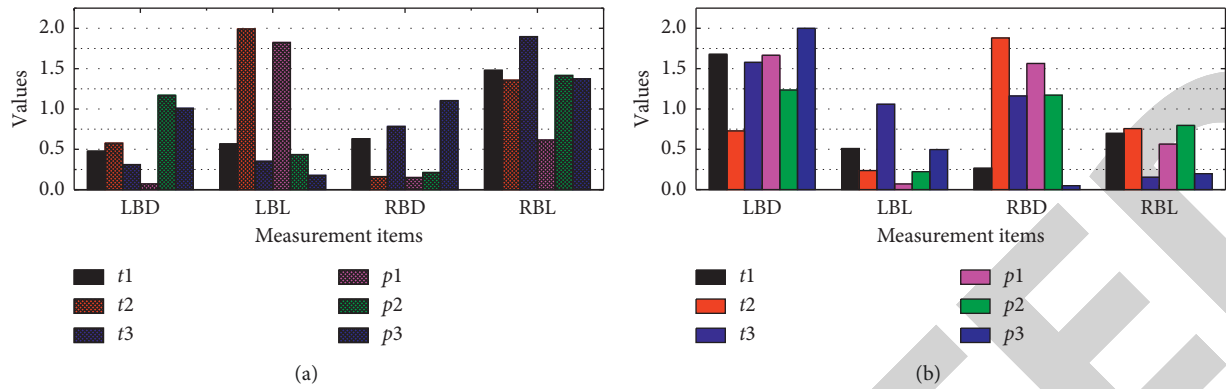


FIGURE 9: Statistical graph of test results.

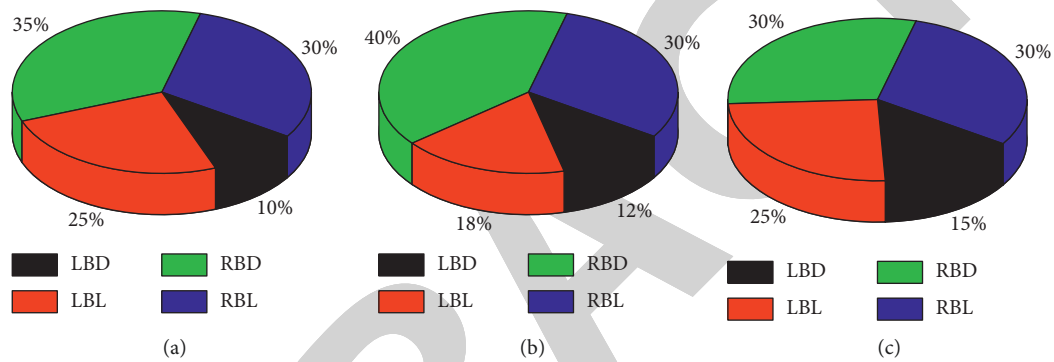


FIGURE 10: Patient VAS scores at each node before and after surgery.

of the orthotropic position of the positioning clamp, and upload it to the robot operation console for registration and matching, and the robot swings the working arm to the best position designed before the operation, cuts the skin and deep fascia along the sleeve, and then proceeds to the next step. After muscle expansion and equalization of the entry point, the guidewire is placed percutaneously along the dentate fixation cannula, the pedicle screw guide wire is placed under x-ray guidance, the skin, subcutaneous tissue, and deep fascia are cut along the entry point of the guidewire on the affected side, the medial multifidus muscle and the longest lateral muscle space are bluntly separated, and the Quadrant channel is placed along with this space. If necessary, microscopic decompression can be used to assist in decompression. The nucleus pulposus and endplate of cartilage can be treated with spatula and nucleus pulposus forceps, intervertebral bone grafting can be performed, and an intervertebral fusion of appropriate size can be inserted. The screws and pedicle joint protrusion screws are removed, the wound is irrigated, sutured layer by layer, and drainage tubes are placed. After incising the skin and subcutaneous fascia, select an appropriate angle and nail entry point to insert a grammar needle percutaneously, continuously adjust the direction under x-ray guidance, replace the grammar needle with a guidewire after reaching the proper position, and screw in the appropriate hollow screw along the guidewire. The pedicle screws were placed under x-ray

guidance on the contralateral side. Except for the difference in the way of nail placement, the two groups were identical in terms of channel placement, decompression, and bone grafting, as shown in Figure 9.

All patients in both groups were followed up, with an average follow-up time of 12.3 months. One patient in group B had cerebrospinal fluid leakage due to tearing of the dura during decompression, and the drainage tube was removed smoothly after intensive rehydration and anti-infection treatment. From the quality of life-related scale, the VAS score and ODI index of lumbar and leg pain in both groups A and B were significantly improved compared with the preoperative evaluation, and the difference was statistically significant ($p < 0.05$); the VAS score and ODI index of lumbar and leg pain in both groups were not significantly improved compared with the preoperative and postoperative follow-up time points. Statistical differences ($p > 0.05$) are shown in Figure 10.

In the present study, CT scans of the head and spine of experimental dogs were performed to obtain cross-sectional, sagittal, coronal, and volume reproduction images and the anatomical locations on the images were annotated. This study has many limitations: firstly, the sample size is relatively small; secondly, the disease activity has not been confirmed by pathology; also, this study only involves subchondral bone marrow signal changes; other inflammatory lesions (such as synovitis, attachment point

inflammation, and joint space inflammation) are not involved in this study; some studies have shown that, for the sensitivity of joint space signal changes, the enhanced images are superior to STIR images.

4. Conclusion

In this paper, we analysed the clinical value of CT scans for the early diagnosis and treatment of spinal fracture and paraplegia. The proposed DMML-Net successfully solves the three challenges of multi-objective, multi-scale, and multi-task through K-means clustering, feature enhancement, multi-scale learning, and multi-task learning modules. To better demonstrate the model's assumptions in selecting appropriate output layers, this paper visualizes the representation of the four output layers generated after processing by the feature enhancement module. Each row corresponds to one output layer, and these generated feature maps are based on a patient's MR image. These can validate the assumptions behind multi-scale learning in this paper and demonstrate the advantages and effectiveness of DMML-Net. A weakly supervised framework combining deep learning and symbolic program synthesis can be used to generate spinal radiology reports very efficiently. In generating diagnostic reports, this paper uses object segmentation rather than object detection because segmentation better represents the spatial correlation between spinal structures. This study is only an attempt, and further work will focus on considering more uncommon spinal disorders and collecting more clinical data to enable end-to-end report generation. In this paper, the DMML-Net algorithm is proposed for automatic localization and classification of spinal disease lesions. The newly proposed automation framework, DMML-Net, paves the way for automated computer-aided diagnosis of spinal disorders and can be applied to automated analysis of other organs.

Data Availability

The data used to support the findings of this study are available from the corresponding author upon request.

Conflicts of Interest

The authors declare that they have no known conflicts of interest or personal relationships that could have appeared to influence the work reported in this paper.

References

- [1] P. Kaur, G. Singh, and P. Kaur, "An intelligent validation system for diagnostic and prognosis of ultrasound fetal growth analysis using neuro-fuzzy based on genetic algorithm," *Egyptian Informatics Journal*, vol. 20, no. 1, pp. 55–87, 2019.
- [2] C. Wang, Z. Li, N. Dey et al., "Histogram of oriented gradient based plantar pressure image feature extraction and classification employing fuzzy support vector machine," *Journal of Medical Imaging and Health Informatics*, vol. 8, no. 4, pp. 842–854, 2018.
- [3] N. Nanda, P. Kakkar, and S. Nagpal, "Computer-aided segmentation of liver lesions in CT scans using cascaded convolutional neural networks and genetically optimised classifier," *Arabian Journal for Science and Engineering*, vol. 44, no. 4, pp. 4049–4062, 2019.
- [4] I. Sangaiah and A. V. A. Kumar, "Improving medical diagnosis performance using hybrid feature selection via relieve and entropy based genetic search (RF-EGA) approach: application to breast cancer prediction," *Cluster Computing*, vol. 22, no. 3, pp. 6899–6906, 2019.
- [5] C. Salem, D. Azar, and S. Tokajian, "An image processing and genetic algorithm-based approach for the detection of melanoma in patients," *Methods of Information in Medicine*, vol. 57, no. 1, pp. 74–80, 2018.
- [6] S. L. Aarthy and S. Prabu, "Tri-texture feature extraction and region growing-level set segmentation in breast cancer diagnosis," *International Journal of Biomedical Engineering and Technology*, vol. 26, no. 3-4, pp. 279–303, 2018.
- [7] A. Victor and M. R. Ghalib, "Detection of skin cancer cells-a review," *Research Journal of Pharmacy and Technology*, vol. 10, no. 11, pp. 4093–4098, 2017.
- [8] M. N. Sudha and S. Selvarajan, "Hybrid approach towards feature selection for breast tumour classification from screening mammograms," *International Journal of Biomedical Engineering and Technology*, vol. 29, no. 4, pp. 309–326, 2019.
- [9] M. Kurkure and A. Thakare, "Classification of stages of lung cancer using genetic candidate group search approach," *IOSR Journal of Computer Engineering*, vol. 18, no. 05, pp. 07–13, 2016.
- [10] L. Yang and Z. Xu, "Feature extraction by PCA and diagnosis of breast tumors using SVM with DE-based parameter tuning," *International Journal of Machine Learning and Cybernetics*, vol. 10, no. 3, pp. 591–601, 2019.
- [11] Y.-K. Chan, M.-J. Chang, Y.-W. Hung et al., "Tissue section image-based liver scar detection," *Journal of Medical and Biological Engineering*, vol. 38, no. 6, pp. 857–866, 2018.
- [12] R. V. Patil, S. S. Sannakki, and V. S. Rajpurohit, "A survey on classification of liver diseases using image processing and data mining techniques," *International Journal of Computer Sciences and Engineering*, vol. 5, no. 3, pp. 29–34, 2017.
- [13] T. Liu, W. Zhang, P. McLean, M. Ueland, S. L. Forbes, and S. W. Su, "Electronic nose-based odor classification using genetic algorithms and fuzzy support vector machines," *International Journal of Fuzzy Systems*, vol. 20, no. 4, pp. 1309–1320, 2018.
- [14] A. Das, P. Das, S. S. Panda, and S. Sabut, "Adaptive fuzzy clustering-based texture analysis for classifying liver cancer in abdominal CT images," *International Journal of Computational Biology and Drug Design*, vol. 11, no. 3, pp. 192–208, 2018.
- [15] J. Rawat, A. Singh, B. Hs, J. Virmani, and J. S. Devgun, "Computer assisted classification framework for prediction of acute lymphoblastic and acute myeloblastic leukemia," *Bio-cybernetics and Biomedical Engineering*, vol. 37, no. 4, pp. 637–654, 2017.
- [16] M. Allam and M. Nandhini, "A study on optimization techniques in feature selection for medical image analysis," *International Journal on Computer Science and Engineering (IJCSSE)*, vol. 9, no. 3, pp. 75–82, 2017.
- [17] R. Mankar, M. J. Walsh, R. Bhargava, S. Prasad, and D. Mayerich, "Selecting optimal features from Fourier

- transform infrared spectroscopy for discrete-frequency imaging,” *The Analyst*, vol. 143, no. 5, pp. 1147–1156, 2018.
- [18] A. Lakshmi, T. Arivoli, and M. Pallikonda Rajasekaran, “A novel M-ACA-based tumor segmentation and DAPP feature extraction with PPCSO-PKC-based MRI classification,” *Arabian Journal for Science and Engineering*, vol. 43, no. 12, pp. 7095–7111, 2018.
- [19] S. Ronoud and S. Asadi, “An evolutionary deep belief network extreme learning-based for breast cancer diagnosis,” *Soft Computing*, vol. 23, no. 24, pp. 13139–13159, 2019.
- [20] R. d. L. Thomaz, P. C. Carneiro, J. E. Bonin, T. A. A. Macedo, A. C. Patrocínio, and A. B. Soares, “Novel mahalanobis-based feature selection improves one-class classification of early hepatocellular carcinoma,” *Medical & Biological Engineering & Computing*, vol. 56, no. 5, pp. 817–832, 2018.
- [21] G. Sethi and B. S. Saini, “Computer aided diagnosis system for abdomen diseases in computed tomography images,” *Bio-cybernetics and Biomedical Engineering*, vol. 36, no. 1, pp. 42–55, 2016.
- [22] Z. Han, B. Wei, A. Mercado, S. Leung, and S. Li, “Spine-gan: semantic segmentation of multiple spinal structures,” *Medical Image Analysis*, vol. 50, pp. 23–35, 2018.